Intrinsic ferroelectricity in Y-doped HfO_2 thin films

Yu Yun,[1†] Pratyush Buragohain,[1†] Ming Li,[1†] Zahra Ahmadi,[2] Yizhi Zhang,[3] Xin Li,[1] Haohan Wang,[1] Jing Li,[1] Ping Lu,[4] Lingling Tao,[1] Haiyan Wang,[3] Jeffrey E. Shield,[2,5] Evgeny Y. Tsymbal,[1,5]* Alexei Gruverman,[1,5]* Xiaoshan Xu[1,5]*

[1] Department of Physics and Astronomy, University of Nebraska-Lincoln, Lincoln, Nebraska 68588, USA
[2] Department of Mechanical and Materials Engineering, University of Nebraska–Lincoln, Lincoln, Nebraska 68588, USA
[3] School of Materials Engineering, Purdue University, West Lafayette, Indiana 47907, USA
[4]Sandia National Laboratories, Albuquerque, NM 87185, USA
[5] Nebraska Center for Materials and Nanoscience, University of Nebraska, Lincoln, Nebraska 68588, USA

†Joint first authors.

*Corresponding authors: tsymbal@unl.edu, agruverman2@unl.edu, xiaoshan.xu@unl.edu

Abstract

Ferroelectric HfO_2-based materials hold great potential for widespread integration of ferroelectricity into modern electronics due to their compatibility with the existing Si technology. Earlier work indicated that the nanometer grain size was crucial for stabilization of the ferroelectric phase of hafnia. This constraint, associated with a high density of structural defects obscures an insight into the intrinsic ferroelectricity of the HfO_2-based materials. Here, we demonstrate that, contrary to the common belief, a stable and significantly enhanced polarization can be achieved in the epitaxial HfO_2 films with high degree of structural order (crystallinity). A record high out-of-plane polarization value of 50 $\mu C/cm^2$ has been observed at room temperature in the Y-doped HfO_2 (111) epitaxial thin films. The estimated full value of the intrinsic polarization is as high as 64 $\mu C/cm^2$, which is in close agreement with the value obtained by density-functional theory (DFT) calculations. The crystal structure of the films reveals the $Pca2_1$ orthorhombic phase with a small rhombohedral distortion, underlining the role of the structural constraint in stabilizing the ferroelectric phase. Our results open a pathway to exploiting the intrinsic ferroelectricity of the HfO_2-based materials and optimizing their performance in device applications.

Introduction

Ferroelectric materials exhibit switchable spontaneous polarization, which makes them promising for application in modern electronics, especially for information storage and processing [1]. However, conventional ABO_3 perovskite ferroelectrics suffer from incompatibility with the current Si-based technology [2-5]. The recent discovery of robust ferroelectricity in the hafnium oxide (HfO_2) based films, which have long been used as high-k dielectrics in the electronic applications, opens a possibility of developing fully integrated ferroelectric devices with markedly improved performance.[6,7]

A core issue for the HfO_2-based ferroelectrics is the stabilization of the otherwise metastable ferroelectric orthorhombic structural phase ($Pca2_1$, *o*-phase, Fig. 1a). All the stable structural phases of HfO_2, i.e., the monoclinic phase ($P2_1/c$, *m*-phase) at room temperature, the tetragonal phase ($P4_2/mnc$, *t*-phase) above 2100 K, and the cubic phase (Fm-3m, *c*-phase) above 2800 K [8] are not ferroelectric. It is commonly accepted that formation of the ferroelectric phase in hafnia favors small grains both as a mechanism of lowering the energy of the ferroelectric phase[10,17-21], and as a result of kinetic stabilization via fast cooling[19,21-32]. The small grain sizes reduce crystallinity (the degree of structural order) and are expected to obscure manifestation of intrinsic ferroelectricity.[9] Indeed, it has been challenging to elucidate the crystal structure of the ferroelectric *o*-phase. To date, most of the experimentally observed spontaneous polarization values are significantly lower than the theoretically predicted ones (40-60 $\mu C/cm^2$) [10-14]. In addition, there are indications that the measured polarization values could be substantially affected by the extrinsic contributions.[15,16]

On the other hand, if the stability of the *o*-phase can be enhanced by additional mechanisms, the ferroelectricity may reconcile with high crystallinity in HfO_2-based materials, allow manifestation of intrinsic properties, and enable better performance in device applications.

In this work, we challenge the common belief that the smaller grain size is required to stabilize the ferroelectric *o*-phase in HfO_2-based thin films. We investigate molar 5% $YO_{1.5}$ doped HfO_2 (YHO) epitaxial thin films with (111) orientation and demonstrate that the ferroelectric polarization actually increases with crystallinity, consistent with a structural-constraint mechanism of stabilizing the *o*-phase. High crystallinity is achieved by optimizing the growth conditions and substrate symmetry and leads to the record-high polarization which is shown to be intrinsic to the ferroelectricity of the *o*-phase hafnia.

Results and Discussion

Positive correlation between P_r and crystallinity

A typical ω-2θ x-ray diffraction (XRD) scan for YHO (111) /LSMO (001)/ STO (001) thin films (≈ 10 nm) grown at substrate temperature T_s = 890 °C in O_2 pressure of P_{O2} = 70 mTorr (optimal condition for polarization, shown below) is shown in Fig. 1b, where LSMO and STO stand for $La_{0.7}Sr_{0.3}MnO_3$ and $SrTiO_3$, respectively. The clear Laue oscillations around the YHO peak indicate smooth surface and interfaces. The peak at $2\theta \approx 30°$ can be assigned to the diffraction of the pseudo cubic $(111)_{pc}$ plane [26-30,33].

Figure 1c shows the Polarization-Voltage (*P*-*V*) loop measured using the positive up and negative down (PUND) method at room temperature for the YHO films grown at optimal condition.

The remanent polarization (P_r) is approximately 36 μC/cm^2, which is larger than all polarization values previously reported for Y-doped HfO_2 films.[22-24,34-36]

The crystallinity of the films was characterized using XRD rocking curves, which measure the lateral coherence length and the crystallite tilt. As shown in Fig. 1d (see also Fig. S2), the rocking curves consist of a sharp peak sitting on a broad peak, corresponding to parts of the films of high (~0.1º tilt, ~100 nm lateral coherence) and low (~1º tilt, ~10 nm lateral coherence) crystallinity respectively (see Fig. S8). We therefore use the sharp/broad peak area ratio to describe the overall crystallinity of the films.

To elucidate whether the high crystallinity contributes to the large P_r, we studied YHO films with different growth temperature T_s, which is expected to be critical for the microstructure of the HfO_2-based films with multiple competing phases;[29] P_{O2} is fixed at 70 mTorr. As T_s changes, the rocking curves (Fig. S2) remain comprised of the sharp peak and the broad peak while their relative weight changes dramatically, indicating change of crystallinity. The T_s dependence of the crystallinity (sharp/broad peak area ratio) shows a non-monotonic trend, with a peak at T_s = 890°C, as shown in Fig. 1e. Below 890°C, the crystallinity increases with temperature, most probably due to the disappearance of the trace of *m*-phase indicated by the $(-111)_m$ peak at $2\theta \approx 28.5°$ (Fig. S1). Above 890°C, the crystallinity decreases with temperature, likely due to the decay of the LSMO layer (Fig. S3). The T_s-dependence of P_r tracks the T_s-dependence of crystallinity perfectly.

To confirm the positive correlation between crystallinity and P_r, we studied YHO films grown on LSMO(110) / STO(110) substrates which has lower (2-fold) rotational symmetry, compared with the 4-fold rotational symmetry of LSMO(001) / STO(001). It turns out, the YHO epitaxial films also grow along the (111) direction, as shown in Fig. 1b. At the optimal growth condition, the YHO(111) / LSMO(110) films also show clear Laue oscillations indicating the sharp surface and interfaces; the P_r reaches ≈ 50 μC/cm^2, as displayed in Fig. 1c. The rocking curve of the films displayed in Fig. 1d is dominated by the sharp peak, indicating high crystallinity. Combining the data of YHO(111) films grown on LSMO(001) and those on LSMO(110), a clear positive correlation can be observed in Fig. 1f between the crystallinity and P_r. Overall, P_r increases with the crystallinity and appears to saturate at a value close to 50 μC/cm^2.

Further confirmation of the positive correlation between crystallinity and P_r is obtained in the P_{O2} dependence study. As shown in Fig. S4, at the optimal P_{O2} = 70 mTorr, the crystallinity is also maximized. Electron microscopy and spectroscopy (Fig. S5) reveal that non-optimal P_{O2} leads low crystallinity and disordered local environment of Hf.

Intrinsic ferroelectric polarization

To cross-check ferroelectricity, the YHO films were studied using piezoresponse force microscopy (PFM) as well as temperature-dependent measurements of the polarization hysteresis loops.

Figures 2a,b show PFM images of the bipolar domain patterns written by an electrically biased tip on the YHO(111) / LSMO(001) film surface. An enhanced PFM amplitude signal was obtained in the electrically poled regions (inside the square marked with blue dashed lines in Fig. 2a). Clear and well-defined domain walls could be seen on the boundary separating the oppositely

poled regions. The corresponding PFM phase images in Fig. 2b reveal bright and dark regions with a nearly 180° phase contrast, corresponding to the downward and upward polarization states, respectively. From the uniform contrast in the PFM amplitude and phase images of the unpoled region, it can be deduced that the polarization in the as-grown film was aligned downward. Comparison of the PFM images with the corresponding topography of the scanned region (Fig. 2c) reveal negligible correlation of the domain patterns and topographic features. Clear terraces and steps in the topography image reveal the high quality of the YHO film. Local PFM spectroscopic measurements (Fig. 2d) demonstrate the electrical switchability of the films. Based upon the clear signature of ferroelectricity obtained from the structural and macroscopic electrical measurements, the observed PFM features are most likely related to the intrinsic ferroelectric behavior, which is not obscured by contribution from the extrinsic factors such as charge injection [37].

Figure 3a shows the *P-V* loops for the YHO(111) /LSMO(001) films grown at the optimal condition, with a weak temperature dependence between 20 and 300 K. For the YHO(111) /LSMO(110) films grown at the optimal condition, the P_r increased from 37 μC/cm^2 at 20 K to about 50 μC/cm^2 at 300 K as shown in Fig. 3b. Comparison of the temperature dependence of P_r for the two different films is shown in Fig. 3c. The increase of P_r with temperature is opposite to that of the conventional ferroelectric materials since the ferroelectric order is expected to be higher at low temperature. One possibility is the extrinsic contributions to the polarization switching process such as oxygen migration [15,38]. Recently, it was reported that most of the polarization in the HZO(111) / LSMO(001) structures could be attributed to oxygen vacancy migration,[15] with the intrinsic ferroelectric polarization estimated to be less than 9 μC/cm^2, where HZO stands for $Hf_{0.5}Zr_{0.5}O_2$. In addition, it was reported that P_r in the HZO films grown on LSMO/$LaNiO_3$/CeO_2/YSZ/Si(100) decreases by a factor of 3 from 300 K to 20 K.[16] On the other hand, for the YHO(111) films studied in this work, P_r exhibits a large value at low temperature and stays nearly constant below 100 K. This suggests that the extrinsic contributions are minimal to the measured P_r at low temperature. The moderate overall change of P_r with temperature also indicates that the contribution from the intrinsic ferroelectricity dominates even at room temperature.

Further evidence for the minimal effect of the oxygen vacancies migration was obtained by comparing the imprint behavior at 300 K (Fig. S11a) and at 20 K (Fig. S11b,c). Recently, it was reported that the imprint in HfO_2-based films is strongly dependent on their poling history, i.e., positive (negative) imprint would develop if the last switching pulse would set the capacitor to the upward (downward) polarization state [39]. This so-called fluid imprint could also be observed in our samples at room temperature (Fig. S11a). However, upon cooling to 20 K, the imprint remained 'frozen-in', which can be attributed to the minimal movement of internal charges (such as oxygen vacancies) at low temperatures.

Finally, *P-V* loops were measured at 20 K for the YHO(111) /LSMO(001) samples with different crystallinity, to verify if the trend of increasing P_r with crystallinity was intrinsic in origin. As shown in Fig. 3d, strong correlation between the high P_r and high crystallinity observed at room temperature could be reproduced at 20 K (see also Fig. 1f), suggesting the intrinsic nature of the observed features.

$Pca2_1$ *o*-phase with a rhombohedral distortion and the *t*→*o* structural transition

The high crystallinity of the YHO films allows for determination of the crystal structure, which is critical for understanding the ferroelectricity. Previously, the ferroelectric HZO(111) / LSMO(001) films have been found to be the *o*-phase [27-29]. Other work identifies a rhombohedral unit cell or possibly a rhombohedral phase in HZO(111) / LSMO(001) [21,26,33]. Here we show that the YHO(111) films grown on both LSMO(110) and LSMO(001) are consistent with the $Pca2_1$ *o*-phase with a rhombohedral distortion, according to the observed lattice constants and distortions.

The lattice constants of the YHO were probed by measuring the spacing of the $\{200\}_{pc}$ planes. For the YHO(111) / LSMO(001) films, due to the 4-fold rotational symmetry of LSMO (001), the YHO(111) films contain four structural domains [33,40], which multiplies the three tilted $\{200\}_{pc}$ planes (tilt angle $\chi \approx 55°$) to twelve (see Fig. S15a). As shown in Fig. 4a, after averaging the twelve directions, the $\{200\}_{pc}$ diffraction profiles show two distinct peaks, corresponding to lattice constants of 5.20 ± 0.01 and 5.07 ± 0.01 Å, respectively. Overall, the peak at smaller 2θ has about ½ of the area of the other peak, indicating that one lattice constant (a) is 5.20 Å, while the other two lattice constants (b and c) are 5.07 Å (see Table 1), because the structural factors of the three $\{200\}_{pc}$ planes are similar due to the nearly cubic structure. The substantial difference between a and $\{b, c\}$ but very close value between b and c is consistent with the orthorhombic $Pca2_1$ structure[10,11,41].

For the YHO(111) / LSMO(110) films, the 2-fold rotational symmetry of LSMO (110) surface generates two structural domains (see Fig. S15b). Since the structural domain boundaries are like "built-in" defects of the films which reduces the crystallinity, the less structural domains in the YHO(111) / LSMO(110) films may explain their higher crystallinity compared with that in the YHO(111) / LSMO(001) films. The double-peaks feature has also been observed for the $\{200\}_{pc}$ planes (Fig. 4a), corresponding to lattice constants $a = 5.21 \pm 0.01$ Å and $b \approx c = 5.08 \pm 0.01$ Å.

Besides the lattice constants, the *o*-phase distinguishes from the *t*-phase and the *m*-phase with a two-fold screw axis along the polar (c) axis and two glide planes perpendicular to the other two axes (a and b), resulting in two lattice distortions patterns (displacement of Hf sites) relative to the *t*-phase (Fig. 4b, c), allowing the diffraction of the orthorhombic $\{010\}_o$ and $\{110\}_o$ planes which are absent for the *t*-phase.

As shown in Fig. 4d, unlike that of the $\{200\}_{pc}$ planes, the diffraction of the $\{100\}_{pc}$ planes only show one peak, corresponding to plane spacings of 5.07 ± 0.01 Å and 5.11 ± 0.01 Å for the YHO(111) / LSMO(001) and the YHO(111) / LSMO(110) films, respectively; both are closer to smaller lattice constants b or c, which is consistent with the $\{010\}_o$ plane and the Hf displacement in Fig. 4b.

The Hf displacement in Fig. 4c has been verified using the diffraction of the $\{110\}_{pc}$ planes ($\chi \approx 35°$). As shown in Fig. 4e, for both the YHO(111) / LSMO(001) and the YHO(111) / LSMO(110) films, only one diffraction peak appears for the $\{110\}_{pc}$ planes, corresponding to spacings of 3.64 ± 0.01 Å and 3.65 ± 0.01 Å, respectively, consistent with the $\{110\}_o$ planes and the Hf displacement in Fig. 4c. Notice that the *m*-phase allows diffraction of both $\{110\}_m$ and $\{011\}_m$ planes, which is expected to show as double peaks of similar intensity.

We measured the temperature dependence of the $\{1\text{-}10\}_{pc}$ diffraction peak using reflection high energy electron diffraction (RHEED) to determine the *t*→*o* phase transition in YHO films, as done previously using XRD[42,43]. As shown in Fig. 4f, both the $(1\text{-}10)_{pc}$ and the $(11\text{-}2)_{pc}$ diffraction intensities appear as weak streaks in the RHEED images at room temperature. As shown in Fig. 4g, at high temperature, the $(1\text{-}10)_{pc}$ diffraction is absent while the $(11\text{-}2)_{pc}$ diffraction peak is present, indicating the *t* phase. When the film was cooled, the $(1\text{-}10)_{pc}$ peak appears at about 450 °C, while the intensity of the $(11\text{-}2)_{pc}$ diffraction peak also increases, indicating a transition to the *o*-phase, which is consistent with the range of transition temperature 350 to 550 °C found in previous studies on YHO [25,42-44].

The rhombohedral distortion was measured from the difference between the spacing of the (111) plane (normal pointing out of the film plane) and that of the tilted $\{111\}_{pc}$, i.e., $(-111)_{pc}$, $(1\text{-}11)_{pc}$ and $(11\text{-}1)_{pc}$ planes, following the work on HZO(111) films.[26,33]

Fig. 4h displays the 2θ scans of the tilted $\{111\}_{pc}$ planes ($\chi \approx 71°$) of the YHO(111) / LSMO(001) films averaged over the four domains. The diffraction peak positions of all the tilted $\{111\}_{pc}$ planes are approximately the same, and well separated from that of the $(111)_{pc}$ plane parallel to the film surface (see Fig. S17, 18 and 19); this indicates a rhombohedral distortion angle -0.41+/-0.04°, similar with the result obtained on HZO(111) / LSMO(001) in the literature. [26,33] As shown in Fig. 4i, the YHO(111) / LSMO(110) films also exhibit a rhombohedral distortion angle -0.25+/-0.02°.

Limited effect of the rhombohedral distortion by theoretical modeling

To explore the effects of the rhombohedral distortion on the structural stability and ferroelectric polarization of the YHO, we performed density-functional theory (DFT) calculations [45]. We started from the orthorhombic $Pca2_1$ unit cell of undoped HfO_2 where the interaxial angles were $\alpha = \beta = \gamma = 90°$. A small rhombohedral distortion was then introduced by reducing the angles while keeping them equal, i.e., $\alpha = \beta = \gamma < 90°$. The experimental values of the lattice parameters were assumed and fixed to be $a = c = 5.07$ Å and $b = 5.20$ Å, and only inner atomic positions were relaxed. Similar calculations were also performed for the 5% Y-doped HfO_2, where effects of doping were modelled by the Virtual Crystal Approximation [46] (see Methods for details).

We find that rhombohedral distortion of the orthorhombic phase enhances the total energy of both the undoped and Y-doped HfO_2 (Fig. 5a) slightly. The total energy is increased only by about 6 meV per unit cell with the angle α being reduced from 90° to 89.6° corresponding to our XRD data. This result indicates that the rhombohedral distortion occurring in our experiment does not minimize the bulk total energy of the grown YHO directly. It is a consequence of the anisotropic constraint imposed by the substrate. The calculated ferroelectric polarization of the orthorhombic $Pca2_1$ phase of HfO_2 is about 50.2 $\mu C/cm^2$, which is consistent with the previous theoretical studies.[10-14] The polarization is directed along the *c*-axis, as enforced by the symmetry of the crystal, so that the *a*- and *b*- components of polarization are zero. The 5% Y doping slightly reduces the polarization down to about 49.9 $\mu C/cm^2$, which indicates that Y does not play a decisive intrinsic role in high polarization values observed in our experiments, but rather helps to stabilize the orthorhombic $Pca2_1$ phase of hafnia.

Figure 5b shows the calculated *c*-component of the ferroelectric polarization P_c as a function of angle α. With a larger rhombohedral distortion (smaller α), the P_c remains large, but slightly reduces. This reduction is just ~ 0.1 μC/cm^2 for the degree of distortion relevant to our experiment. At the same time the broken $Pca2_1$ symmetry allows the appearance of non-vanishing *a*- and *b*- components of polarization, P_a and P_b (see Fig. S21d). Y-doped HfO_2 exhibits the same tendency as the pristine HfO_2 (compare the red and blue lines in Fig. 5b), implying an idle role of the doping in the polarization enhancement.

Overall, our DFT calculations reveal that the rhombohedral distortion observed in our experiments is not intrinsic to the bulk HfO_2 and most likely results from the structural constraint imposed by the substrate. In addition, the rhombohedral distortion of the degree observed in our experiments does not much affect the large ferroelectric polarization value of the orthorhombic $Pca2_1$ phase of the pristine and YHO.

Importantly, comparing the results of our DFT calculations and experimental data indicates that we observe the intrinsic ferroelectricity of YHO at low temperature. Experimentally, the remanent polarization saturates with increasing crystallinity at low temperature values ranging from 32 μC/cm^2 to 37 μC/cm^2, corresponding to the YHO(111) grown on LSMO(001) and LSMO(110), respectively (Fig. 1f). For the $Pca2_1$ *o*-phase, these values represent the projection of polarization of YHO pointing along the *c* axis onto the out-of-plane $(111)_{pc}$ direction, which is consistent with our measurements of in-plane polarization that show comparable P_r (Fig. S20). This implies that the total spontaneous polarization along the *c* axis is in the range from 55 μC/cm^2 to 64 μC/cm^2, which is in good agreement with the results of our DFT calculations.

Discussion

Contrary to the common expectation, we demonstrate a positive crystallinity-P_r correlation in the YHO(111) thin films. Compared with earlier studies on epitaxial thin films, this correlation guides us to maximize crystallinity and achieve intrinsic record-high polarizations.

The positive crystallinity-P_r correlation requires a mechanism of *o*-phase stabilization that favors high crystallinity and does not need small grain size. A recent theoretical work [21] proposes a structural-constraint mechanism in the (111) oriented hafnia thin films. Essentially, the *t*→*m* transition requires much larger and more uneven changes of lattice constants and angles and a much larger (4%) volume expansion compared with that of the *t*→o transition [10]. Under the constraint of fixed (111) plane, the *t*→*m* transition is suppressed because of the much-increased *m*-phase energy associated with the large uneven changes of lattice constants and angles. Any residual volume expansion manifests in the rhombohedral distortion along the out-of-plane (111) direction, as illustrated in Fig. 5c. This mechanism does not require reduced grain size. In fact, low crystallinity, i.e., large tilt and smaller lateral coherence length of the (111) plane, is expected to weaken the constraint and lead to the *m*-phase impurity which is consistent with the observation in Fig. S1. Hence, the structural constraint mechanism is likely to play a major role in stabilizing the *o*-phase in the YHO(111) films studied in this work.

Summary and Outlook

We have demonstrated that the commonly accepted rule that the stabilization of the ferroelectric $Pca2_1$ structure of hafnia favors reduced grain sizes, can be relaxed, by showing the

positive crystallinity-P_r correlation in the YHO(111) films. This finding has significant implications in fundamental materials science for clarifying the crystal structure and polarization intrinsic to the ferroelectric hafnia. We show that in YHO(111) films of high crystallinity, the polarization is as high as the theoretical prediction down to the low temperature, indicating intrinsic origin. We also show that the rhombohedral hafnia phase previously proposed and difficult to explain could actually be the theoretically predicted orthorhombic phase with a small rhombohedral distortion due to the structural constraint. The relaxation of the rule of reduced grain sizes also has important impact on application of ferroelectric hafnia. For YHO(111) films of high crystallinity, we show that the extrinsic factors that compromise ferroelectric properties such as polarization, switching speed, and endurance, are minimized. We expect this work to mark a milestone in understanding the intrinsic properties of the HfO_2-based ferroelectric materials and a critical step toward developing fully integrated ferroelectric devices, taking advantage of the large polarization, compatibility with Si technology, and environmental friendliness.

References

1 Scott, J. F. *Ferroelectric Memories*. (Springer Press, 2000).

2 Kushida-Abdelghafar, K., Miki, H., Torii, K. & Fujisaki, Y. Electrode-induced degradation of $Pb(Zr_xTi_{1-x})O_3$ (PZT) polarization hysteresis characteristics in Pt/PZT/Pt ferroelectric thin-film capacitors. *Appl. Phys. Lett.* **69**, 3188-3190 (1996).

3 Shimamoto, Y., Kushida-Abdelghafar, K., Miki, H. & Fujisaki, Y. H_2 damage of ferroelectric $Pb(Zr,Ti)O_3$ thin-film capacitors—The role of catalytic and adsorptive activity of the top electrode. *Appl. Phys. Lett.* **70**, 3096-3097 (1997).

4 Aggarwal, S. *et al.* Effect of hydrogen on $Pb(Zr,Ti)O_3$-based ferroelectric capacitors. *Appl. Phys. Lett.* **73**, 1973-1975 (1998).

5 Ma, T. P. & Han, J.-P. Why is Nonvolatile Ferroelectric Memory Field-Effect Transistor Still Elusive? *IEEE Electron Device lett.* **23**, 386-388 (2002).

6 Böscke, T. S., Müller, J., Bräuhaus, D., Schröder, U. & Böttger, U. Ferroelectricity in hafnium oxide thin films. *Appl. Phys. Lett.* **99**, 102903 (2011).

7 Mikolajick, T., Slesazeck, S., Park, M. H. & Schroeder, U. Ferroelectric hafnium oxide for ferroelectric random-access memories and ferroelectric field-effect transistors. *MRS Bull.* **43**, 340-346 (2018).

8 J. WANG, H. P. LI & STEVENS, R. Hafnia and hafnia-toughened ceramics. *J. Mater. Sci.* **27**, 5397-5430 (1992).

9 Chouprik, A., Negrov, D., Tsymbal, E. Y. & Zenkevich, A. Defects in ferroelectric HfO_2. *Nanoscale* **13**, 11635-11678 (2021).

10 Materlik, R., Künneth, C. & Kersch, A. The origin of ferroelectricity in $Hf_{1-x}Zr_xO_2$: A computational investigation and a surface energy model. *J. Appl. Phys.* **117**, 134109 (2015).

11 Lee, H. J. *et al.* Scale-free ferroelectricity induced by flat phonon bands in HfO_2. *Science* **369**, 1343-1347 (2020).

12 Qi, Y. *et al.* Stabilization of Competing Ferroelectric Phases of HfO_2 under Epitaxial Strain. *Phys. Rev. Lett.* **125**, 257603 (2020).

13 Cao, J., Shi, S., Zhu, Y. & Chen, J. An Overview of Ferroelectric Hafnia and Epitaxial Growth. *Phys. Status. Solidi. Rapid. Res. Lett.* **15**, 2100025 (2021).

14 Kashir, A., Kim, H., Oh, S. & Hwang, H. Large Remnant Polarization in a Wake-Up Free $Hf_{0.5}Zr_{0.5}O_2$ Ferroelectric Film through Bulk and Interface Engineering. *ACS Appl. Electron. Mater.* **3**, 629-638 (2021).

15 Nukala, P. *et al.* Reversible oxygen migration and phase transitions in hafnia-based ferroelectric devices. *Science* **372**, 630-635 (2021).

16 Adkins, J. W., Fina, I., Sánchez, F., Bakaul, S. R. & Abiade, J. T. Thermal evolution of ferroelectric behavior in epitaxial $Hf_{0.5}Zr_{0.5}O_2$. *Appl. Phys. Lett.* **117**, 142902 (2020).

17 Park, M. H. *et al.* Evolution of phases and ferroelectric properties of thin $Hf_{0.5}Zr_{0.5}O_2$ films according to the thickness and annealing temperature. *Appl. Phys. Lett.* **102**, 242905 (2013).

18 Park, M. H. *et al.* Surface and grain boundary energy as the key enabler of ferroelectricity in nanoscale hafnia-zirconia: a comparison of model and experiment. *Nanoscale* **9**, 9973-9986 (2017).

19 Park, M. H. *et al.* Understanding the formation of the metastable ferroelectric phase in hafnia-zirconia solid solution thin films. *Nanoscale* **10**, 716-725 (2018).

20 Batra, R., Tran, H. D. & Ramprasad, R. Stabilization of metastable phases in hafnia owing to surface energy effects. *Appl. Phys. Lett.* **108**, 172902 (2016).

21 Liu, S. & Hanrahan, B. M. Effects of growth orientations and epitaxial strains on phase stability of HfO_2 thin films. *Phys. Rev. Mater.* **3**, 054404 (2019).

22 Xu, X. *et al.* Kinetically stabilized ferroelectricity in bulk single-crystalline HfO_2:Y. *Nat. Mater.* **20**, 826-832 (2021).
23 Katayama, K. *et al.* Growth of (111)-oriented epitaxial and textured ferroelectric Y-doped HfO_2 films for downscaled devices. *Appl. Phys. Lett.* **109**, 112901 (2016).
24 Katayama, K. *et al.* Orientation control and domain structure analysis of {100}-oriented epitaxial ferroelectric orthorhombic HfO2-based thin films. *J. Appl. Phys.* **119**, 134101 (2016).
25 Shimizu, T. *et al.* The demonstration of significant ferroelectricity in epitaxial Y-doped HfO_2 film. *Sci. Rep.* **6**, 32931 (2016).
26 Wei, Y. F. *et al.* A rhombohedral ferroelectric phase in epitaxially strained $Hf_{0.5}Zr_{0.5}O_2$ thin films. *Nat. Mater.* **17**, 1095-1100 (2018).
27 Yoong, H. Y. *et al.* Epitaxial Ferroelectric $Hf_{0.5}Zr_{0.5}O_2$ Thin Films and Their Implementations in Memristors for Brain-Inspired Computing. *Adv. Funct. Mater.* **28**, 1806037 (2018).
28 Estandia, S. *et al.* Engineering Ferroelectric $Hf_{0.5}Zr_{0.5}O_2$ Thin Films by Epitaxial Stress. *ACS Appl. Electron. Mater.* **1**, 1449-1457 (2019).
29 Lyu, J., Fina, I., Solanas, R., Fontcuberta, J. & Sanchez, F. Growth Window of Ferroelectric Epitaxial $Hf_{0.5}Zr_{0.5}O_2$ Thin Films. *ACS Appl. Electron. Mater.* **1**, 220-228 (2019).
30 Bégon-Lours, L. *et al.* Stabilization of phase-pure rhombohedral $HfZrO_4$ in pulsed laser deposited thin films. *Phys. Rev. Mater.* **4**, 043401 (2020).
31 Park, M. H. *et al.* Ferroelectricity and Antiferroelectricity of Doped Thin HfO_2-Based Films. *Adv. Mater.* **27**, 1811-1831 (2015).
32 Song, T. *et al.* Epitaxial Ferroelectric La-Doped $Hf_{0.5}Zr_{0.5}O_2$ Thin Films. *ACS Appl. Electron. Mater.* **2**, 3221-3232 (2020).
33 Nukala, P. *et al.* Guidelines for the stabilization of a polar rhombohedral phase in epitaxial $Hf_{0.5}Zr_{0.5}O_2$ thin films. *Ferroelectrics* **569**, 148-163 (2020).
34 Mimura, T., Shimizu, T., Uchida, H., Sakata, O. & Funakubo, H. Thickness-dependent crystal structure and electric properties of epitaxial ferroelectric Y_2O_3-HfO_2 films. *Appl. Phys. Lett.* **113**, 102901 (2018).
35 Mimura, T., Shimizu, T. & Funakubo, H. Ferroelectricity in $YO_{1.5}$-HfO_2 films around 1 μm in thickness. *Appl. Phys. Lett.* **115**, 032901 (2019).
36 Shimura, R. *et al.* Preparation of near-1-μm-thick {100}-oriented epitaxial Y-doped HfO_2 ferroelectric films on (100)Si substrates by a radio-frequency magnetron sputtering method. *J. Ceram. Soc. JAPAN* **128**, 539-543 (2020).
37 Vasudevan, R. K., Balke, N., Maksymovych, P., Jesse, S. & Kalinin, S. V. Ferroelectric or non-ferroelectric: Why so many materials exhibit "ferroelectricity" on the nanoscale. *Appl. Phys. Rev.* **4**, 021302 (2017).
38 Lee, J. S., Lee, S. & Noh, T. W. Resistive switching phenomena: A review of statistical physics approaches. *Appl. Phys. Rev.* **2**, 031303 (2015).
39 Buragohain, P. *et al.* Fluid Imprint and Inertial Switching in Ferroelectric La:HfO_2 Capacitors. *ACS Appl. Mater. Interfaces* **11**, 35115-35121 (2019).
40 Estandía, S., Dix, N., Chisholm, M. F., Fina, I. & Sánchez, F. Domain-Matching Epitaxy of Ferroelectric $Hf_{0.5}Zr_{0.5}O_2$(111) on $La_{2/3}Sr_{1/3}MnO_3$(001). *Cryst. Growth Des.* **20**, 3801−3806 (2020).
41 Sang, X., Grimley, E. D., Schenk, T., Schroeder, U. & LeBeau, J. M. On the structural origins of ferroelectricity in HfO_2 thin films. *Appl. Phys. Lett.* **106**, 162905 (2015).
42 Mimura, T. *et al.* Effects of heat treatment and in situ high-temperature X-ray diffraction study on the formation of ferroelectric epitaxial Y-doped HfO_2 film. *Jpn. J. Appl. Phys.* **58**, SBBB09 (2019).

43 Tashiro, Y., Shimizu, T., Mimura, T. & Funakubo, H. Comprehensive Study on the Kinetic Formation of the Orthorhombic Ferroelectric Phase in Epitaxial Y-Doped Ferroelectric HfO_2 Thin Films. *ACS Appl. Electron. Mater.* **3**, 3123-3130 (2021).
44 Shimizu, T. *et al.* Growth of epitaxial orthorhombic $YO_{1.5}$-substituted HfO_2 thin film. *Appl. Phys. Lett.* **107**, 032910 (2015).
45 Giannozzi, P. *et al.* QUANTUM ESPRESSO: a modular and open-source software project for quantum simulations of materials. *J. Phys. Condens. Matter.* **21**, 395502 (2009).
46 J. D. Burton & Tsymbal, E. Y. Prediction of electrically induced magnetic reconstruction at the manganite/ferroelectric interface. *Phys. Rev. B* **80**, 174406 (2009).

Methods

Sample preparation. The YHO thin films on $La_{0.7}Sr_{0.3}MnO_3$ (LSMO) bottom electrodes were grown by pulse laser deposition (PLD) with a wavelength of 248 nm on $SrTiO_3$ (STO) substrates. The base pressure of PLD chamber is around 3×10^{-7} mTorr. Before depositions, the STO substrates were pre-annealed at 650°C for 1 hour in PLD chamber. LSMO layer with thickness of ~25 nm was deposited at 600°C under a 60 mTorr oxygen atmosphere. The ceramic 5% Y-doped HfO_2 target was synthesized at 1400°C by solid-state reaction using HfO_2 (99.99% purity) and Y_2O_3 (99.9% purity) powders. The growth temperature from 750°C to 970°C, a repetition rate of 2 Hz and an oxygen pressure of 70 mTorr were employed to grow the YHO films. The typical thickness of YHO films is about 9-11 nm. At the end of deposition, the temperature of the films decreases to room temperature with a cooling rate of 10°C/min under an oxygen pressure of 70 mTorr. The platinum top electrodes with thickness of ~15 nm were deposited ex-situ by PLD using shadow mask in vacuum at room temperature. The diameter of top electrodes is from 75 μm to 400 μm.

X-ray structural characterization. The structural characterizations, including XRD θ-2θ scans, rocking curves and x-ray reflectivity (XRR), were performed by XRD (Rigaku SmartLab Diffractometer) using Cu Kalpha (wavelength ~ 1.54 Å). The IP and OOP d-spacing of the $\{111\}$ planes and that of the $\{001\}$, $\{002\}$, and $\{110\}$ planes in YHO films were measured using an area detector (Bruker-AXS D8 Discover Diffractometer, wavelength ~ 1.54 Å).

Electrical measurements. For the measurements of the ferroelectric properties at room temperature, a solid Pt tip (RMN-25PT400B, RockyMountain Nanotechnology) in contact with the platinum top electrode was used to apply the voltage pulses using a Keysight 33621A arbitrary waveform generator while the transient switching currents through the bottom electrode were recorded by a Tektronix TDS 3014B oscilloscope. In all measurements, the bias was applied to the top electrode (diameter from 75 μm to 400 μm) while the LSMO bottom electrode was grounded. The low-temperature measurements with temperature range from 20 K to 300 K are implemented using Cryostat, Sumitomo Cryogenics, and the top electrodes are connected using silver paint and silver wires.

Scanning probe microscopy. PFM measurements were carried out using a commercial AFM system (MFP-3D, Asylum Research) using Pt-coated tips (PPP-EFM, Nanosensor) in the resonance tracking mode by applying an ac modulation signal of 0.8 V amplitude and a frequency of ~ 350 kHz. The bias was applied through the conductive tip and the bottom electrode was grounded.

Electron microscopy. For the images with the view along YHO $[1\bar{1}0]$ (same as LSMO [001]): The TEM foil was prepared by conventional cutting, grinding and polishing followed by a precision ion polishing (Gatan PIPS695 tool). (S)TEM images with EDS mappings were obtained by a high-resolution transmission electron microscope (HRTEM) FEI TALOS-F200X equipped with high-angle annular dark-field (HAADF) detectors and energy dispersive X-ray spectrometer (EDX). For the images with the view along YHO $[11\bar{2}]$ (same as LSMO $[1\bar{1}0]$): An electron transparent cross section of sample of HfO_2/LSMO thin film on STO substrate was prepared using Helios NanoLab Dual Beam 660 SEM. The cross-section sample was mounted on a copper FIB lift-out grid. The thinning of the cross-section sample was started from the bottom of the sample to avoid damaging the top part of the sample where the thin films were deposited. Thus, sample

was tilted 52±7°, 52±5°, 52±3°, 52±1.5° and was thinned from 2 μm to less than 100 nm by ion beam with 15 kV and 0.42 nA, 8 kV and 0.23 nA, 5 kV 80 pA, and 3 kV and 20 pA, respectively. The final polishing was done at 2 kV and 20 pA. The sample was characterized using a FEI Tecnai Osiris S/TEM. To understand the oxygen impact, the film microstructure was also characterized by a scanning transmission electron microscope (STEM, FEI Titan G2 80-200) operated at 200 kV. Electron energy-loss spectroscopy (EELS, GATAN 963) was used to probe the O fine structure of the YHO films under the following optical parameters: an electron probe of size < 0.13 nm, convergence angle of 18.1 mrad, collection angle of 15 mrad, energy dispersion 0.25 eV/channel, and instantaneous dwell time of 500 ms. High-angle annular dark-field (HAADF) images were recorded under similar optical conditions and using an annular detector with a collection range of 60-160 mrad.

Density-functional theory (DFT) calculations. First-principles DFT calculations were performed using the plane-wave pseudopotential method implemented in the Quantum-ESPRESSO package [45]. Generalized gradient approximation (GGA) for the exchange and correlation functional and an energy cutoff of 544 eV were used in the calculations. The atomic relaxations were performed with an 8×8×8 k-point mesh until the Hellmann-Feynman forces on each atom became less than 1.3 meV/Å. A 10×10×10 k-point mesh was used for the subsequent self-consistent calculations. The Berry phase method was applied to calculate the ferroelectric polarization. The effects of Y doping was modelled by Virtual Crystal Approximation (VCA) [46], by simulating each Hf-site with a pseudopotential of fractional valence. To neutralize the charge in the structures, O-sites are also treated by VCA.

Data availability

The data that support the findings of this study are included in the main text and Supplementary Information.

References

47 Chierchia, R. *et al.* Microstructure of heteroepitaxial GaN revealed by x-ray diffraction. *J. Appl. Phys.* **93**, 8918-8925 (2003).

48 Lee, H. G. *et al.* Double-layer buffer template to grow commensurate epitaxial $BaBiO_3$ thin films. *APL Mater.* **4**, 126106 (2016).

49 Marcaud, G. *et al.* High-quality crystalline yttria-stabilized-zirconia thin layer for photonic applications. *Phys. Rev. Mater.* **2**, 035202 (2018).

50 Heying, B. *et al.* Role of threading dislocation structure on the x-ray diffraction peak widths in epitaxial GaN films. *Appl. Phys. Lett.* **68**, 643-645 (1996).

51 Islamov, D. R. *et al.* Identification of the nature of traps involved in the field cycling of $Hf_{0.5}Zr_{0.5}O_2$-based ferroelectric thin films. *Acta Mater.* **166**, 47-55 (2019).

52 Y. W. So, D. J. Kim, Noh, T. W., Yoon, J.-G. & Song, T. K. Polarization switching kinetics of epitaxial $Pb(Zr_{0.4}Ti_{0.6})O_3$ thin films. *Appl. Phys. Lett.* **86**, 092905 (2005).

53 Lia, W. & Alexe, M. Investigation on switching kinetics in epitaxial $Pb(Zr_{0.2}Ti_{0.8})O_3$ ferroelectric thin films: Role of the 90° domain walls. *Appl. Phys. Lett.* **91**, 262903 (2007).

54 Daniel Pantel *et al.* Switching kinetics in $BiFeO_3$ epitaxial films. *J. Appl. Phys.* **107**, 084111 (2010).

Acknowledgements

This work was primarily supported by the National Science Foundation (NSF), Division of Electrical, Communications and Cyber Systems (ECCS) under Grant No. ECCS-1917635. The research was performed in part in the Nebraska Nanoscale Facility: National Nanotechnology Coordinated Infrastructure and the Nebraska Center for Materials and Nanoscience, which are supported by the NSF under Grant No. ECCS- 2025298, and the Nebraska Research Initiative. Y.Z. and H.W. acknowledge the support from NSF (DMR-2016453 and DMR-1565822 for the microscopy effort at Purdue University. Sandia National Laboratories is a multimission laboratory managed and operated by National Technology and Engineering Solutions of Sandia, LLC., a wholly owned subsidiary of Honeywell International, Inc., for the U.S. Department of Energy's National Nuclear Security Administration under contract DE-NA0003525. This paper describes objective technical results and analysis. Any subjective views or opinions that might be expressed in the paper do not necessarily represent the views of the U.S. Department of Energy or the United States Government.

Author contributions

The thin films were synthesized by Y.Y. with the assistance from X.X. and Hao.W. Structure distortion and symmetry were investigated by Y.Y. and X.X. Time-resolved RHEED was studied by Y.Y. and X.L. The local switching and temperature-dependent polarization were studied and analyzed by P.B. under the supervision of A.G. M.L. carried out the DFT calculations under the supervision of L.T. and E.Y.T. (S)TEM experiments were conducted by Z.A. and Y.Z. under the supervision of J.S. P.L. and Hai.W., respectively. The study was conceived by Y.Y., P.B. and X.X. Y.Y., P.B., M.L., E.Y.T., A.G. and X.X. co-wrote the manuscript. All authors discussed results and commented on the manuscript.

Competing interests

The authors declare no competing interests.

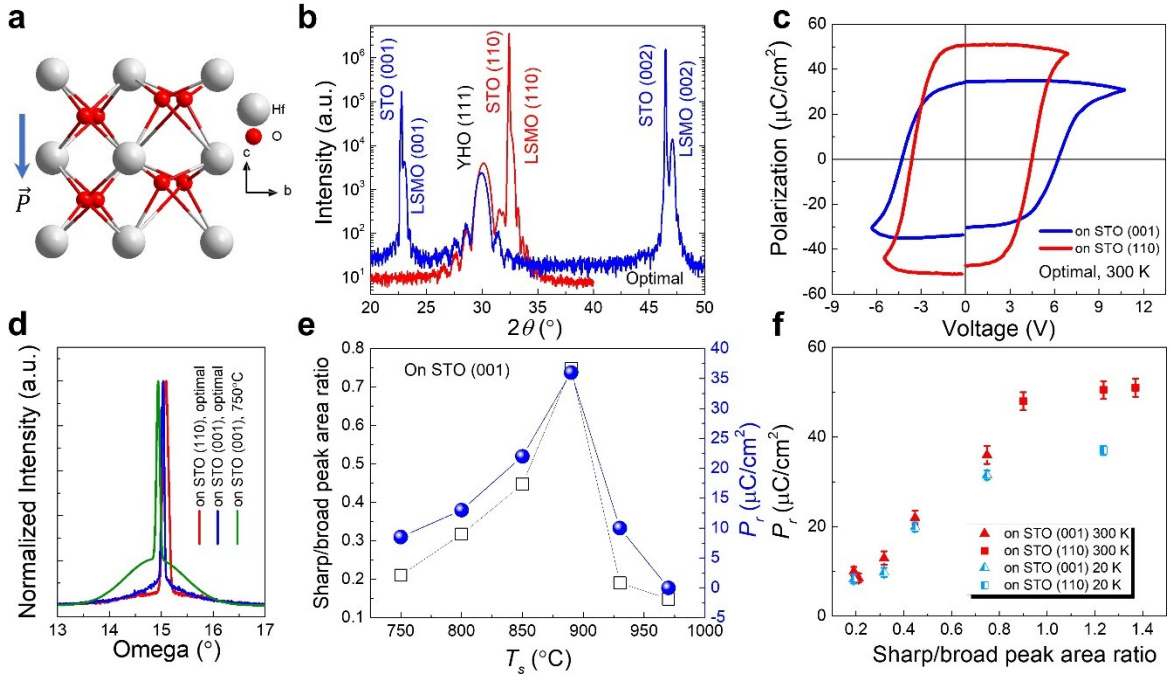

Fig. 1 | Structure characterization and ferroelectric hysteresis. a, Crystal structure of HfO_2 with $Pca2_1$ space group and a downward polarization. **b,** ω-2θ XRD scan of YHO(111) grown on LSMO(001)/STO(001) and on LSMO(110)/ STO(110) respectively. **c,** Typical *P*-*V* loops of YHO(111) / LSMO(001) and YHO(111) / LSMO(110) measured at 300K respectively. **d,** Rocking curves of the YHO(111) peaks. **e,** Growth temperature (T_s) dependence of the large/small grain ratio (squares) and the remanent polarization (P_r) (blue circles) for the YHO/LSMO/STO(001) films. **f,** Remanent polarization (P_r) as a function of sharp/broad peak area ratio at 20K (blue symbols) and 300K (red symbols) on LSMO(111) (triangles) and on LSMO (squares).

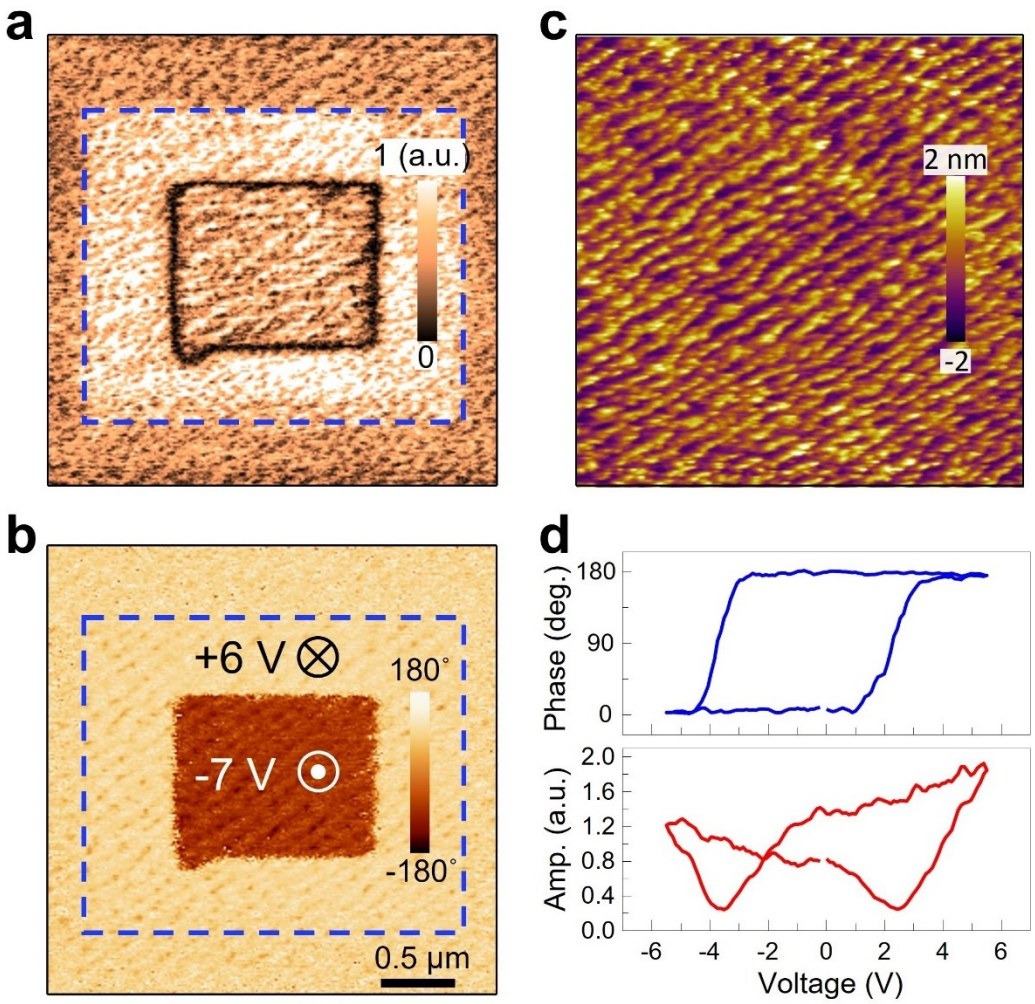

Fig. 2 | Local ferroelectric switching by PFM. a, Magnitude and **b,** phase of the PFM image after poling with +6V and -7V, demonstrating stable, bipolar, remanent polarization states. **c,** AFM image of the surface of the YHO(111) / LSMO(001) film, displaying the atomic step-and-terrace morphology. **d,** Phase and amplitude switching spectroscopy loops, demonstrating ferroelectric-like hysteresis on bare surface.

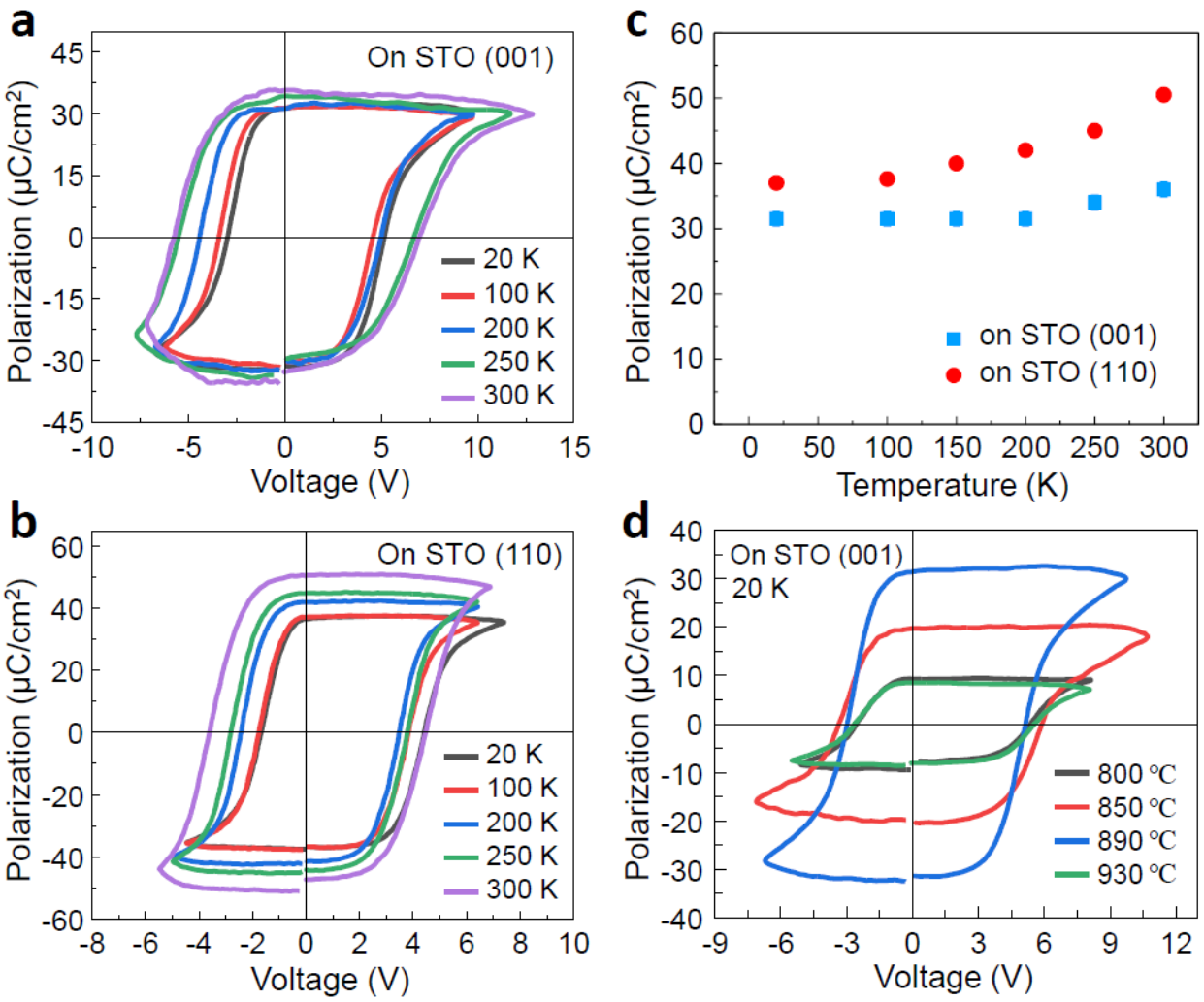

Fig. 3 | Temperature dependence of the ferroelectric hysteresis. Ferroelectric *P-V* loops measured by the PUND methods at temperature range from 20K to 300K for **a,** YHO(111) / LSMO(001) and **b,** YHO(111) / LSMO(110) grown in optical condition. **c,** Remanent polarization as a function of temperature for YHO(111) / LSMO(001) and YHO(111) / LSMO(110) grown in optical condition. **d,** *P-V* loops for the samples of YHO(111) / LSMO(100) with various growth temperature (T_s) measured at 20K.

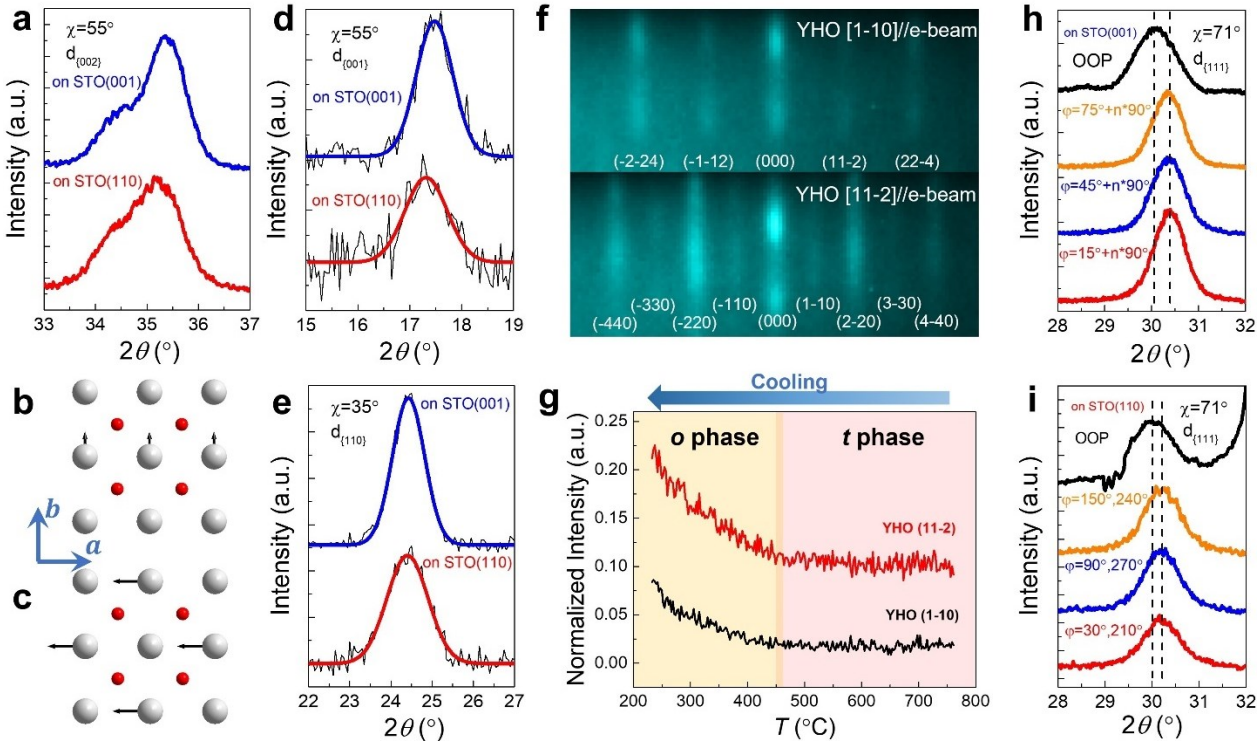

Fig. 4 | Structural characterization of the YHO films. a, The diffraction of the $\{002\}_{pc}$, **d,** $\{001\}_{pc}$ and **e,** $\{110\}_{pc}$ plane with χ=55°, χ=55° and χ=35°, respectively. **b,** and **c,** are the displacement patterns of Hf atoms of the $Pca2_1$ *o*-phase HfO_2. **f,** RHEED pattern of YHO(111) grown on LSMO(110) along the $[1\text{-}10]_{pc}$ and $[11\text{-}2]_{pc}$ directions at room temperature. **g,** Temperature dependence of the RHEED intensity of the $(1\text{-}10)_{pc}$ and the $(11\text{-}2)_{pc}$ streaks, demonstrating a $t \rightarrow o$ phase transition at about 450°C. In-plane and out-of-plane $\{111\}_{pc}$ diffractions for **h,** YHO(111) / LSMO(001) and **i,** YHO(111) / LSMO(110).

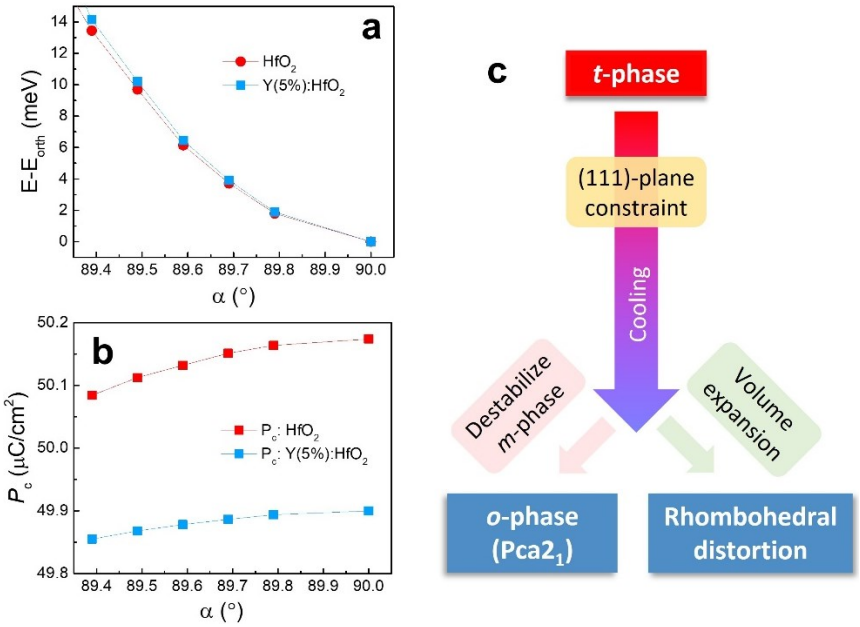

Fig. 5 | Results of DFT calculations for bulk undoped and 5% Y-doped HfO_2. a, Change in the total energy. **b,** Calculated components of the ferroelectric polarization along the *c*-axis (squares) as a function of angle α for bulk undoped HfO_2 (red lines and symbols) and 5% Y-doped HfO_2 (blue lines and symbols). **c,** Schematic diagram of stabilization of the *o*-phase in the YHO(111) films.

Table 1 Structure parameter of YHO(111) films grown on LSMO/STO(001) and LSMO/STO(110) measured by XRD at room temperature.

Substrate	***a* (Å)**	***b*, *c* (Å)**	**Rhombohedral distortion (°)**	**Epitaxial relation**
LSMO (001)	5.20 ± 0.01	5.07 ± 0.01	-0.41 ± 0.04	YHO(111) || LSMO(001) YHO[1-10] || LSMO[1-10]
LSMO (110)	5.21 ± 0.01	5.08 ± 0.01	-0.25 ± 0.02	YHO(111) || LSMO(110) YHO[1-10] || LSMO[001]